Article

Validation of Ash/Dust Detections from SEVIRI Data Using ACTRIS/EARLINET Ground-Based LIDAR Measurements

Alfredo Falconieri [1],* , Nikolaos Papagiannopoulos [1] , Francesco Marchese [1] , Carolina Filizzola [1], Serena Trippetta [1], Nicola Pergola [1] , Gelsomina Pappalardo [1], Valerio Tramutoli [2] and Lucia Mona [1]

1   Consiglio Nazionale delle Ricerche-Istituto di Metodologie per l'Analisi Ambientale, C. da S. Loja, 85050 Tito Scalo (PZ), Italy; nikolaos.papagiannopoulos@imaa.cnr.it (N.P.); francesco.marchese@imaa.cnr.it (F.M.); carolina.filizzola@imaa.cnr.it (C.F.); serena.trippetta@imaa.cnr.it (S.T.); nicola.pergola@imaa.cnr.it (N.P.); gelsomina.pappalardo@imaa.cnr.it (G.P.); lucia.mona@imaa.cnr.it (L.M.)
2   School of Engineering, University of Basilicata, 85100 Potenza, Italy; valerio.tramutoli@unibas.it
*   Correspondence: alfredo.falconieri@imaa.cnr.it; Tel.: +39-0971427273

Abstract: Two tailored configurations of the Robust Satellite Technique (RST) multi-temporal approach, for airborne volcanic ash and desert dust detection, have been tested in the framework of the European Natural Airborne Disaster Information and Coordination System for Aviation (EUNADICS-AV) project. The two algorithms, running on Spinning Enhanced Visible Infra-Red Imager (SEVIRI) data, were previously assessed over wide areas by comparison with independent satellite-based aerosol products. In this study, we present results of a first validation analysis of the above mentioned satellite-based ash/dust products using independent, ground-based observations coming from the European Aerosol Research Lidar Network (EARLINET). The aim is to assess the capabilities of RST-based ash/dust products in providing useful information even at local scale and to verify their applicability as a "trigger" to timely activate EARLINET measurements during airborne hazards. The intense Saharan dust event of May 18–23 2008—which affected both the Mediterranean Basin and Continental Europe—and the strong explosive eruptions of Eyjafjallajökull (Iceland) volcano of April–May 2010, were analyzed as test cases. Our results show that both RST-based algorithms were capable of providing reliable information about the investigated phenomena at specific sites of interest, successfully detecting airborne ash/dust in different geographic regions using both nighttime and daytime SEVIRI data. However, the validation analysis also demonstrates that ash/dust layers remain undetected by satellite in the presence of overlying meteorological clouds and when they are tenuous (i.e., with an integrated backscatter coefficient less than ~0.001 sr^{-1} and with aerosol backscatter coefficient less than ~1×10^{-6} $m^{-1}sr^{-1}$). This preliminary analysis confirms that the continuity of satellite-based observations can be used to timely "trigger" ground-based LIDAR measurements in case of airborne hazard events. Finally, this work confirms that advanced satellite-based detection schemes may provide a relevant contribution to the monitoring of ash/dust phenomena and that the synergistic use of (satellite-based) large scale, continuous and timely records with (ground-based) accurate and quantitative measurements may represent an added value, especially in operational scenarios.

Keywords: ash clouds; dust outbreaks; SEVIRI; EARLINET; RST

1. Introduction

Several studies have shown that satellite systems play a very important role for studying ash/dust clouds thanks to advantages in terms of synoptic view, continuity of observation and availability of multi-spectral data provided at different spatial/temporal scales [1–3].

After a number of pioneering works investigating ash/dust clouds in the visible and infrared bands [4,5], many studies were performed exploiting the reverse absorption effect of silicate-rich particles at around 11 μm and 12 μm wavelengths in comparison with water and ice droplets [6–8]. Ash and dust particles, because of their mineralogical composition and size, exhibit a similar spectral behavior at the aforementioned thermal infrared (TIR) wavelengths, which generally lead to negative values of the BT11-BT12 (where BT is the brightness temperature) spectral difference [6,8,9]. However, fixed threshold tests applied to the brightness temperature difference (BTD) generally fail in detecting ash/dust clouds over some background surfaces (e.g., desert areas), and under different atmospheric/observational conditions (e.g., in the presence of a high amount of atmospheric water vapor [7,10]).

To improve the identification of ash/dust from space, some authors developed methods analyzing the visible (VIS) and/or medium infrared (MIR) radiances collected by sensors such as the advanced very high resolution radiometer (AVHRR) and the moderate resolution imaging spectroradiometer (MODIS) [11–14]. Other authors verified the advantages of using the BT3.7-BT11 [15] and BT8.6-BT11 [16] spectral differences to better detect desert dust aerosols. An enhanced BTD method was recently used to detect ash exploiting the information also from the spinning enhanced visible infrared imager (SEVIRI) channel centered at 8.7 μm wavelength, before characterizing ash plumes from a quantitative point of view [17,18].

Among the methods developed to identify ash/dust plumes from space [18–23], two robust satellite techniques (RST) based algorithms, running on both polar and geostationary satellite data, were used with success in different geographic areas and under different observational conditions [24–29]. These algorithms were tailored in the framework of the European Natural Airborne Disaster Information and Coordination System for Aviation (EUNADICS-AV) project (http://www.eunadics.eu/), which aims at bridging the gap in European-wide data and information availability during airborne hazards.

In this study, we present a validation analysis of RST ash/dust detections against the European Aerosol Research Lidar Network (EARLINET), operating Raman lidars at a continental scale. EARLINET is a unique tool for validation of satellite sensors and algorithms because it provides profiles of quality assured aerosol optical properties [30,31].

Two intense ash/dust events affecting Europe are considered for this first analysis. In particular, the massive Saharan dust episode of May 18–23, 2008, which strongly affected the Mediterranean basin [32], and the significant Eyjafjallajökull (Iceland) eruption of April–May 2010 which caused unprecedented air traffic disruption in Europe [33], are analyzed to assess RST performance at a local scale. These test cases were selected for two reasons. First, both events affected Europe in terms of increased aerosol load and geographic extent. Second, they were extensively investigated using both EARLINET lidar observations [31,34] and the RST detection algorithm [27,35]. In particular, we previously assessed RST ash/dust detections at regional/continental scale, through comparison with some independent and well-established satellite-based aerosol products [25–27]). In this work, RST detections, including those from a tailored algorithm version for ash detection for the first time presented and tested here, are validated at local scale using ground-based data, namely the ground-truth EARLINET lidar measurements.

2. Methods

2.1. RST Detection Scheme

The RST multi-temporal technique uses a local variation index called Absolutely Local Index of Change of Environment (ALICE) to identify anomalous signal variations related to perturbing events [24]:

$$\otimes_V (x, y, t) = \frac{V(x, y, t) - \mu_V(x, y)}{\sigma_V(x, y)}. \tag{1}$$

In Equation (1) $V(x, y, t)$ is the satellite signal measured at time t and location (x, y), $\mu_V(x, y)$ is temporal average and $\sigma(x, y)$ is the temporal standard deviation. These terms are calculated at pixel level, by analyzing plurennial time series of homogeneous (i.e., same spectral channels, same calendar month and overpass times) cloud-free satellite records, after using the iterative $k\sigma$ clipping filter to remove signal outliers. In this work, we implemented the same cloud screening procedure used and described in [27] within the RST process in order to investigate the Saharan dust event of May 2008. The only RST-based method described in [36] was used to filter out meteorological clouds at the high latitude regions (i.e., to investigate the Eyjafjallajökull test case), for the reasons already discussed in [35]. In more detail, to generate the spectral reference fields (i.e., μ_V and σ_V in Equation (1) required to run the RST algorithm configurations detailed below, we processed nine years of SEVIRI data acquired at the School of Engineering of University of Basilicata (UNIBAS) (Italy) receiving station between 2004 and 2012, in several different time slots (i.e., 08:45 UTC; 10:00 UTC; 21:00 UTC for dust; 06:00 UTC; 07:15–08:45 UTC; 12:00 UTC and 18:00 UTC for the ash event).

2.1.1. RST$_{ASH}$ Algorithm

The RST$_{ASH}$ algorithm combines two local variation indices to identify volcanic ash by means of SEVIRI data. These indices are defined as:

$$\otimes_{BT10.8-BT12} (x, y, t) = \frac{[BT10.8(x, y, t) - BT12(x, y, t)] - \mu_{BT10.8-BT12}(x, y)}{\sigma_{BT10.8-BT12}(x, y)}; \tag{2}$$

$$\otimes_{BT3.9-BT10.8} (x, y, t) = \frac{[BT3.9(x, y, t) - BT10.8(x, y, t)] - \mu_{BT3.9-BT10.8}(x, y)}{\sigma_{BT3.9-BT10.8}(x, y)}. \tag{3}$$

In both Equations, all the terms have the same meaning as Equation (1), in reference to the considered wavelength (e.g., $BT3.9(x, y, t)$ is the BT measured in the MIR band at around 3.9 μm wavelength). The RST$_{ASH}$ algorithm was tested with success in previous studies despite some limitations [13,37–39]. To increase the RST$_{ASH}$ efficiency in discriminating ash from meteorological clouds, an improved algorithm configuration tailored to SEVIRI data, integrating an additional index analyzing visible radiance at 0.6 μm wavelength, was experimented with good results in [35]. Here, to reduce artefacts because of weather clouds on both daytime and nighttime scenes, the $\otimes_{BT8.7-BT10.8}$ index is used:

$$\otimes_{BT8.7-BT10.8} (x, y, t) = \frac{[BT8.7(x, y, t) - BT10.8(x, y, t)] - \mu_{BT8.7-BT10.8}(x, y)}{\sigma_{BT8.7-BT10.8}(x, y)}. \tag{4}$$

The index in Equation (4), integrated within the standard RST$_{ASH}$ scheme described above, should further increase the confidence level of ash detection, exploiting the peculiar absorption properties of volcanic plumes in this spectral region. In particular, we used the following algorithm arrangement to identify ash pixels (the first two tests are the same of the standard RST$_{ASH}$ detection scheme).

Ash pixels:

$$\otimes_{BT10.8-BT12} (x, y, t) < -2 \; AND \; \otimes_{BT3.9-BT10.8} (x, y, t) > 1 \; AND \; \otimes_{BT8.7-BT10.8} (x, y, t) < -1.$$

2.1.2. The eRST$_{DUST}$ Algorithm

The RST$_{DUST}$ algorithm uses the index in Equation (2) to identify desert dust aerosols [25]. The enhanced algorithm configuration, which was named *e*RST$_{DUST}$, integrates two other local variation indices for better discriminating dust from meteorological clouds in daylight conditions (in nighttime only the indices (2) and (6) are used) over both land and sea areas [27]:

$$\otimes_{VIS}(x,y,t) = \frac{L_{0.6}(x,y,t) - \mu_{L0.6}(x,y)}{\sigma_{L0.6}(x,y)};$$

(5)

$$\otimes_{BT10.8}(x,y,t) = \frac{BT_{10.8}(x,y,t) - \mu_{BT10.8}(x,y)}{\sigma_{BT10.8}(x,y)}.$$

(6)

In Equation (5) $L_{0.6}(x,y,t)$ is the radiance measured in the visible band of SEVIRI, at around 0.6 μm wavelength, $\mu_{L0.6}(x,y)$ *and* $\mu_{BT10.8}(x,y)$ are the temporal mean, while $\sigma_{L0.6}(x,y)$ and $\sigma_{BT10.8}(x,y)$ stand for the temporal standard deviation. Advantages of using *e*RST$_{DUST}$ in place of the RST$_{DUST}$ algorithm were widely discussed in [27]. Here, we used the *e*RST$_{DUST}$ algorithm to detect dusty pixels on both nighttime and daytime scenes using the same algorithm arrangement detailed in [27].

2.2. EARLINET Ground-Based Lidar Measurements

EARLINET was established in 2000 as a research project, providing data concerning the aerosol vertical distribution on a continental scale [40]. EARLINET has been integrated and represents a major component of the European Research Infrastructure for the observation of Aerosol, Clouds, and Trace Gases (shortly named ACTRIS-Aerosols, Clouds and Trace gases Research InfraStructure Network) [41]. The main objective of EARLINET is to provide profiles of aerosol optical properties at a continental scale. Based on different lidar systems developed typically at research institutes, quality assurance and quality check procedures are a key component of ACTRIS/EARLINET activities for guaranteeing the quality of ACTRIS/EARLINET data.

Currently, 30 active stations participate in the network, the majority of which run Raman lidars equipped with depolarization channels. The Raman-lidar-operating EARLINET stations typically provide profiles of the aerosol extinction and backscatter coefficients without significant assumptions. Simultaneous acquisition of elastic lidar signal (i.e., backscattered signal at the same wavelength of the emitted laser beam) and of the Raman inelastic signal, corresponding to the N_2 molecules, allows for the solution of the lidar equation without assumptions on the aerosol content in the atmosphere. This technique permits a direct measurement of extinction and backscatter coefficient profiles. This is different in respect to the elastic backscatter Cloud-Aerosol Lidar with Orthogonal Polarization (CALIOP) lidar onboard the Cloud-Aerosol Lidar and Infrared Pathfinder Satellite Observation (CALIPSO) satellite, where the aerosol type and the extinction-to-backscatter ratio are assumed for the extinction and backscatter coefficient retrieval.

As stated above, two observational periods are examined referring to a desert dust outbreak and a volcanic plume affecting Europe. The aerosol optical properties profiles are freely available at [40,42] and are published on the CERA database [43,44]. Aerosol features from EARLINET are categorized according to methods already consolidated within the network. In short, the whole process can be described in three steps. First, the aerosol-cloud discrimination is performed. Second the boundary location of the features is determined. Third, the aerosol typing is performed by means of investigation of intensive optical properties (Ångström exponent, lidar ratios, linear particle depolarization ratio), model outputs, backward trajectory analyses, and ancillary instruments data if available [34,45]. In particular, the geometrical properties, the layer extensive/intensive properties, and the aerosol type can be found in the devoted databases.

3. Test Cases

3.1. Saharan Dust Events of May 2008

In May 2008, two intense Saharan dust events affected the Mediterranean basin and Europe. The first episode took place from May 18 to 23, and on the first day the dust plume originating from North Africa affected Italy and Central Europe [32]. The day after, airborne dust dispersed over Eastern Europe covering Greece, where it reached a maximum intensity level on May 20 (dust load reached values around 0.75 g/m^2 [32]). In the following hours, dust concentration progressively decreased. The second dust episode took place from May 27–30, when the dust plume coming from the Sahara was transported towards Central and Northern Europe dispersing up to Scandinavia and the Norwegian Sea [46]. Previous studies investigated these massive dust events by means of satellite and/or ground-based observations [27,35,46–48]. Dust maps from the standard and enhanced RST$_{DUST}$ algorithm were used to investigate the space-time evolution of the dust dispersion, providing information in agreement with that given by the BSC-DREAM8b model [27].

3.2. Eyjafjallajökull Ash Events of April–May 2010

In April 2010, an explosive eruption of the Eyjafjallajökull volcano (Iceland) injected a significant amount of volcanic ash into the atmosphere (the average ash mass concentration was estimated to be no more than 170 μg m^{-3} [49]). The eruption caused, from April 15 to 20, unprecedented air traffic disruption in Europe leading to huge economic losses for the aviation industry, which were estimated at a hundred million dollars per day, and the distress of millions of stranded passengers [50,51]. Specifically, after the effusive phase occurring in March, a phreatomagmatic eruption started on April 14, emitting fine-grained ash, which reached an altitude of about 10 km a.s.l. (above sea level), causing the airspace closure over most of Europe five days later [52]. On the evening of April 18, when the eruption style changed from phreatomagmatic to magmatic, the first explosive phase ended. A lower amount of ash (extending around 3–5 km a.s.l. and having a coarser size) was emitted [53]. On May 5, the explosive activity resumed, causing the emission of a significant amount of fine ash and pumice. Since May 18, the eruption intensity decreased and the eruptive activity ceased four days later [54].

The Eyjafjallajökull eruption revealed several issues in the operational monitoring and forecasting of ash events [55], encouraging the development of improved methods and procedures capable of better supporting activities devoted to mitigating the impact of ash clouds on air traffic. In this context, the tailored RST$_{ASH}$ product tested here was developed to increase the accuracy of the ash detection, assessing its performance at specific sites of interest.

4. Results

4.1. Validation of Dust Products of May 2008

In this section, we show the results of the validation analysis of the *e*RST$_{DUST}$ detections performed during the period of May 18–23, 2008, against EARLINET by analyzing both nighttime and daytime SEVIRI scenes. The *e*RST$_{DUST}$ products display dusty pixels in two different colors, based on the confidence level of dust detections (brown = high confidence; orange = mid–low confidence; see [27]). In addition, the SEVIRI TIR channel imagery at 10.8 μm wavelength is shown in the background to emphasize areas affected by meteorological clouds (in black/dark grey tones). The EARLINET stations that performed measurements concurrently with the SEVIRI overpass are superimposed on the map with red dots, whereas the rest stations within the same geographic domain are not reported.

Figure 1a displays the *e*RST$_{DUST}$ map from SEVIRI data on May 19 at 21:00 UTC. The map shows that a significant dust plume covered both the Ionian and south Adriatic Sea, also dispersing over part of Southern Italy (e.g., Puglia region), including the town of Potenza (Basilicata region; see orange pixels). Two hours prior to the above-mentioned satellite observation, the Potenza EARLINET site monitored the dust plume, in the 1.4–3.3 km a.s.l. altitude range, for the period 18:45–19:15 UTC

(SEVIRI data in Figure 1a was the closest in time to the EARLINET measurement due to some gaps in data acquisition at the UNIBAS receiving station). The optical profiles (i.e., particle backscatter and extinction coefficient) derived by the multi-wavelength Raman lidar along with the intensive properties (i.e., Ångström exponent and lidar ratio) can be seen in Figure 1b. The mean layer backscatter coefficient at 532 nm is 3.7×10^{-6} m^{-1} sr^{-1} and the mean layer extinction coefficient is 1.9×10^{-4} m^{-1}. The type-specific intensive properties confirmed the presence of mineral particles, with layer-mean Ångström exponent (e.g., the 532 nm and 1064 nm couple) values of 0.6 ± 0.1, and lidar ratio at 532 nm of 52 ± 7 sr [53]. However, the dust layer was mixed with marine particles due to the low flight height over the Mediterranean of the dust cloud.
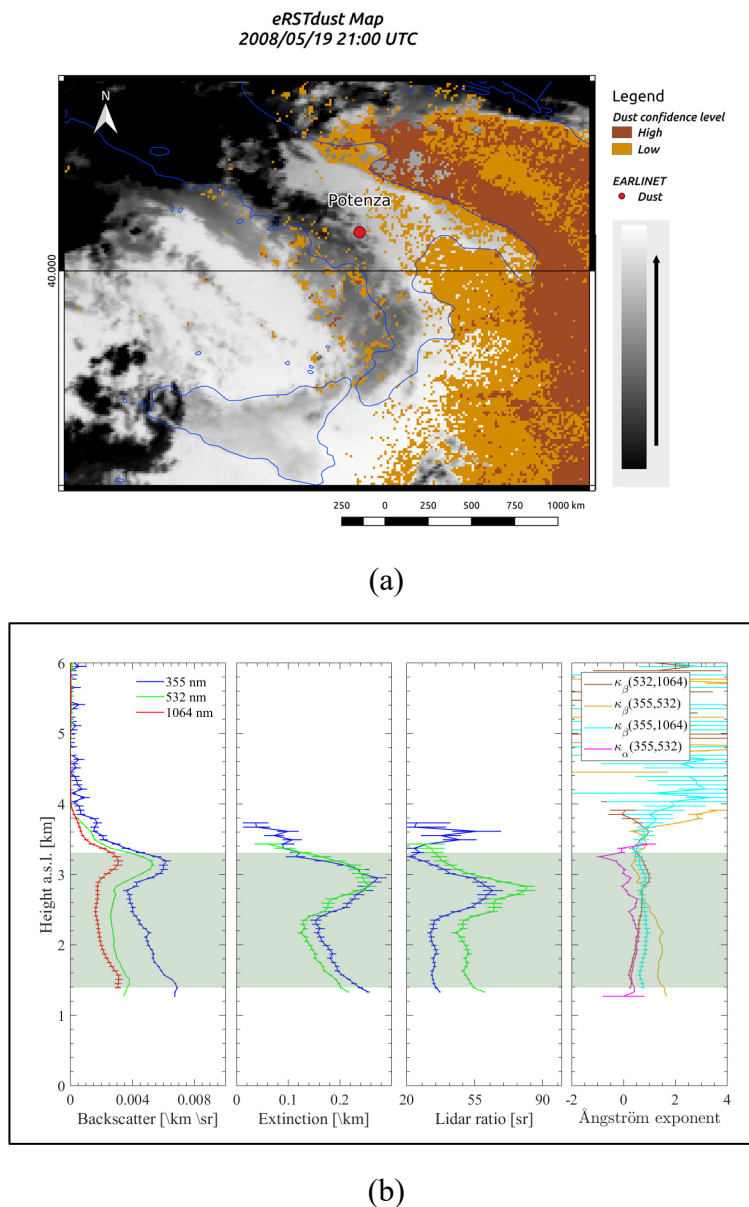

(a)

(b)

Figure 1. (**a**) eRST$_{DUST}$ map from SEVIRI (Spinning Enhanced Visible InfraRed Imager) data of May 19 at 21:00 UTC (magnified over Southern Italy and generated using the same algorithm arrangement of [27]), with the 10.8 μm channel displayed in the background and the red dot indicating the concurrent dust identification of EARLINET (European Aerosol Research Lidar Network) (Potenza station). (**b**) Potenza EARLINET aerosol backscatter coefficient, extinction coefficient, lidar ratio and Ångström exponent profiles acquired the same day between 18:45–19:15 UTC. The green zone indicates the dust-affected portion of the profile.

Figure 2a shows the eRST$_{DUST}$ product of May 20 at 08:45 UTC, which was generated some hours after the previously analyzed SEVIRI data. The map indicates that the airborne dust affected a significant portion of the scene (see high number of flagged dusty pixels). In particular, according to eRST$_{DUST}$ the dust plume, coming from the Sahara Desert, moved from Libya with a northeast direction, spreading over Eastern Europe and affecting Thessaloniki (Greece) and Sofia (Bulgaria; see brown pixels), where EARLINET measurements were available.
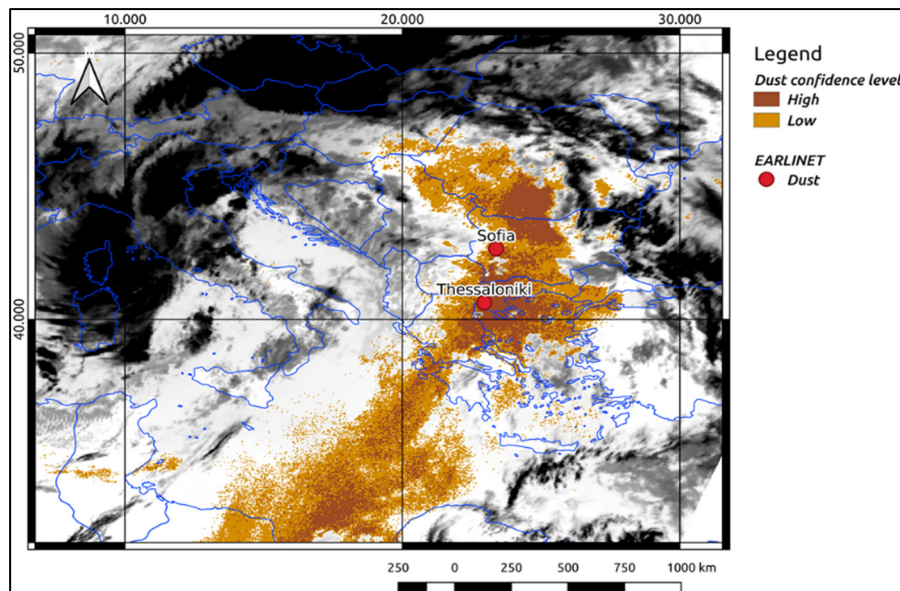
(a)
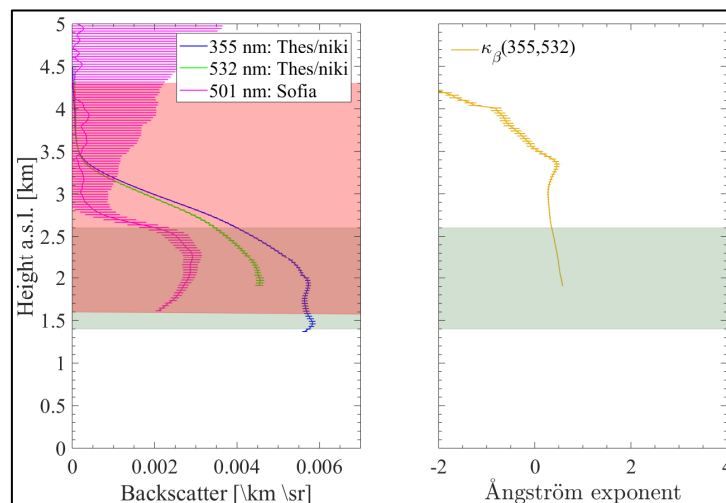
(b)

Figure 2. (**a**) eRST$_{DUST}$ map from SEVIRI data on May 20 at 08:45 UTC. (**b**) Sophia and Thessaloniki EARLINET aerosol backscatter coefficient, and Angstrom exponent profiles acquired the same day between 08:48–09:20 UTC showing a dust layer in the 1.8–4.7 km a.s.l. and 1.4–4.8 km a.s.l. altitude range, respectively (see Figure 3d).

Conversely, in the presence of meteorological clouds residing above the dust plume, the eRST$_{DUST}$ product did not perform the same. Figure 3a displays, for instance, the dust product from SEVIRI data of May 18 at 10:00 UTC generated during the initial stage of the investigated dust episode. The figure shows that eRST$_{DUST}$ did not flag any dusty pixel over Potenza, although concurrent ground-based

lidar measurements reported the existence of dust particles in the 1.8–2.8 km a.s.l. range (see Figure 3b). The mean-layer backscatter coefficient at 532 nm 2.3×10^{-6} m^{-1} sr^{-1}. The Ångström exponent, using the couple 355 nm and 532 nm, was 0.52 ± 0.10, indicating the predominance of coarse particles. The layer was also mixed with smoke from local sources. Above the dust layer, clouds attenuated the lidar signal with a cloud base around 3.4 km a.s.l. Therefore, the eRST$_{DUST}$ algorithm missed the dust layer because of the overlying weather clouds (cloudy pixels affected most of the analyzed satellite scene). Thus, EARLINET measurements confirmed high and thick meteorological clouds as the major factor affecting the efficiency of eRST$_{DUST}$ detections.

Later the same day, the persisting dust plume was observed by the ground-based lidar for the temporal windows 17:50–18:19 UTC but not from space.

The mean backscatter coefficient at 532 nm is 1.6×10^{-6} m^{-1} sr^{-1} and the mean extinction coefficient is 8.3×10^{-5} m^{-1}. The type-specific intensive properties confirmed the presence of mineral particles, with layer-mean Ångström exponent (e.g. 532 nm and 1064 nm) values of 0.52 ± 0.1, and lidar ratio at 532 nm of 53 ± 7 sr. The lidar identified a cirrus cloud in the 7.8–10 km a.s.l. altitude range. The eRST$_{DUST}$ did not identify any dusty pixel over that location once again because of clouds (see SEVIRI data of 21:00 UTC shown in Figure 3c)
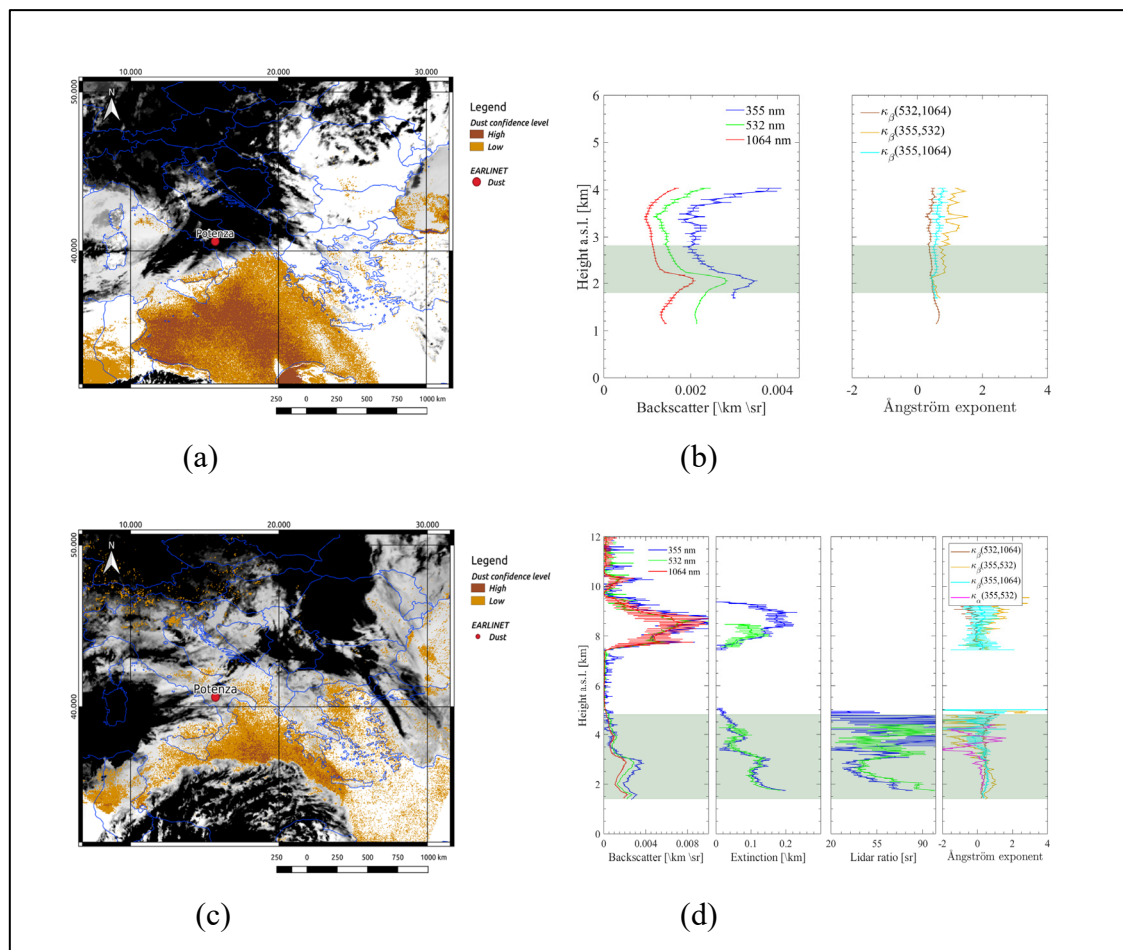

Figure 3. (**a**) eRST$_{DUST}$ map of May 18 at 10:00 UTC. (**b**) Potenza EARLINET aerosol backscatter coefficient and Angstrom exponent profiles acquired the same day between 09:55–10:30 UTC. The green zone indicates the dust affected portion of the profile; (**c**) eRST$_{DUST}$ map of May 18 at 21:00 UTC. (**d**) Potenza EARLINET aerosol backscatter coefficient, extinction coefficient, lidar ratio and Ångström exponent profiles acquired the same day between 21:46–22:15 UTC. The green zone indicates the dust affected portion of the profile.

4.2. Validation of RST$_{ASH}$ Detections of April–May 2010

Figure 4 displays two ash maps generated from the standard (Figure 4a) and tailored RST$_{ASH}$ algorithm (Figure 4b) for April 16, 2010 at 06:00 UTC (i.e., during the first phase of the eruption), when the water-rich plume from the erupting volcano moved towards Europe [33]. We marked in red dots the EARLINET stations reporting the presence of ash (i.e., Hamburg and Payerne), the green dots indicate the EARLINET stations with either no observations or no ash presence. The figure shows that the RST$_{ASH}$ algorithm flagged the presence of ash (see blue pixels) mainly over Northern Europe (North Germany, North Poland and the Baltic Sea). The plume, based on information retrieved from SEVIRI data (both ash products), dispersed over Hamburg (Germany) but did not affect Payerne (Switzerland). The EARLINET stations at the above-mentioned locations observed concurrently the ash cloud in the temporal window 05:30–06:30 UTC (Figure 4c). In particular, over Germany, the ash cloud extended from near the ground (0.7 km a.s.l.) up to 5.2 km a.s.l., with a mean backscatter coefficient at 532 nm of 6.04×10^{-6} m^{-1} sr^{-1}. Over Switzerland, the plume was observed in the 4.5–5.5 km a.s.l. range, with a mean-layer backscatter coefficient of 0.41×10^{-6} m^{-1} sr^{-1} at 355 nm (see Figure 4c). Apparently, the volcanic ash in Germany had a greater impact in the lidar signals in terms of intensity and vertical extent when compared to the Switzerland case. This is also emphasized by the wavelength difference between Hamburg (532 nm) and Payerne (355 nm). Hence, RST$_{ASH}$ did not identify volcanic ash over Payerne, regardless of the algorithm configuration, because of the weaker aerosol layer (i.e., mean-layer backscatter coefficient at 355 nm of 0.41×10^{-6} m^{-1} sr^{-1}). On the other hand, the standard RST$_{ASH}$ algorithm overestimated ash pixels in the south sector of the scene, with respect to the tailored one. In particular, the standard RST$_{ASH}$ product (Figure 4a) flagged a higher number of ash pixels over the Tyrrhenian Sea and Southern Italy than the map of Figure 4b (i.e., the tailored product). These pixels occurred mainly in correspondence with some cloudy areas, as indicated by the manual inspection of satellite imagery. In addition, the EARLINET stations in the central Mediterranean did not report ash particles on April 16 (see EARLINET stations marked in green in Figure 4) although the volcanic cloud was observed within a period of ±2 h from the satellite observation in Leipzig (East Germany), Minsk (Belarus), Neuchatel (Switzerland), and Palaiseau (France) stations. These EARLINET stations were located far from above-mentioned cloudy areas. Therefore, ash pixels flagged over the western Mediterranean classified by the standard RST$_{ASH}$ product represented artefacts. This analysis shows that the tailored RST$_{ASH}$ algorithm (Section 2.1.1) was capable of further reducing false positives in comparison with the standard algorithm configuration. On the other hand, since the tailored RST$_{ASH}$ algorithm was in general slightly less efficient in detecting ash pixels—although it provided the same results as the standard one at the analyzed EARLINET stations—a more extensive comparison between the two algorithm versions is required to better assess differences in detecting ash at different spatial scales. However, this intercomparison is out of the scope of this work and will be discussed in a future paper.

Figure 5a displays the tailored RST$_{ASH}$ product referring to the third phase of the Eyjafjallajökull eruption, when the volcano emitted once again a significant amount of ash (see Section 3.2). In particular, the map generated from SEVIRI data on May 17 at 18:00 UTC shows that a spatially extended ash plume dispersed over the North Sea, affecting the EARLINET station of Cabauw (the Netherlands). Concurrent EARLINET measurements reported the presence of an ash layer in Hamburg where RST$_{ASH}$ did not detect ash pixels (Figure 5a). The ash layer was found in the 1.2–4.9 km a.s.l. range with a mean-layer backscatter coefficient at 532 nm of 0.6×10^{-6} m^{-1}sr^{-1} (Figure 5c). We deduce that RST$_{ASH}$ missed the ash cloud over Hamburg due to the lower intensity (i.e. 0.6×10^{-6} m^{-1}sr^{-1} with respect to the 1.6×10^{-6} m^{-1}sr^{-1} observed over Cabauw). Lidar measurements performed on May 17 over Cabauw between 17:30–18:30 UTC confirmed a strong ash presence in the 3–5.5 km a.s.l. range (EARLINET stations marked in red in Figure 5a). The optical coefficient profiles derived by the multi-wavelength Raman lidar along with the intensive properties (i.e., Ångström exponent and lidar ratio) can be seen in Figure 5b. The mean backscatter coefficient at 532 nm is 1.6×10^{-6} range. m^{-1} sr^{-1}. The layer-mean Ångström exponent (e.g., 532 nm and 1064 nm) value is 0.4.
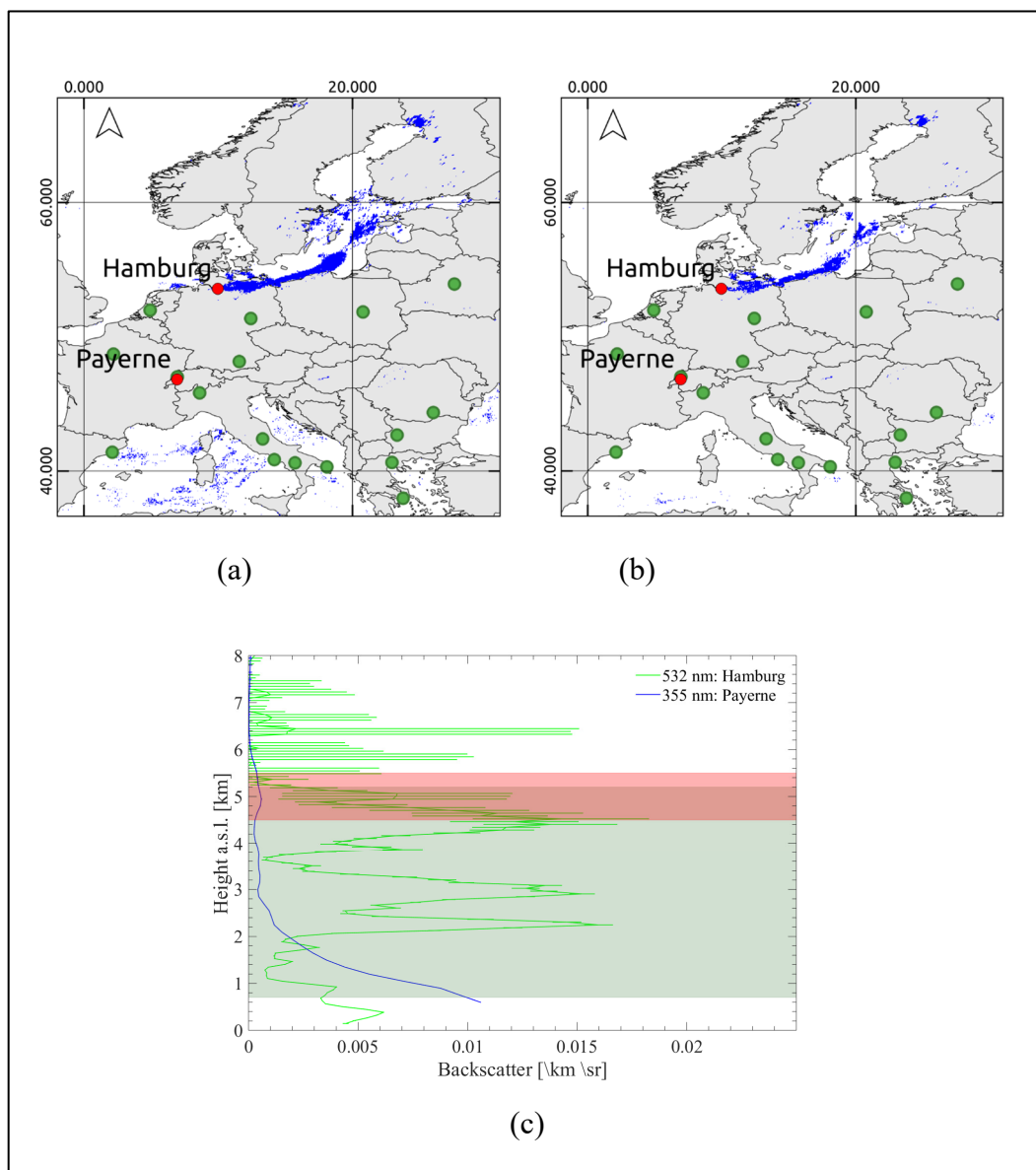
Figure 4. (**a**) Standard RST$_{ASH}$ product of April 16 at 06:00 UTC. (**b**) Tailored RST$_{ASH}$ product of the same day and hour generated using the algorithm arrangement described in Section 2.1.1. EARLINET measurement stations revealing the presence of ash at the time of analyzed SEVIRI data are reported in red and in green sites where no information about the possible presence of ash was available. (**c**) Aerosol backscatter coefficient profile at 532 nm retrieved at the EARLINET station of Hamburg and at 355 nm retrieved at the EARLINET station of Payerne between 05:30–06:30 UTC. The green zone indicates the ash affected portion of the profile of the Hamburg station and the pink zone is referred at the profile of Payerne station.
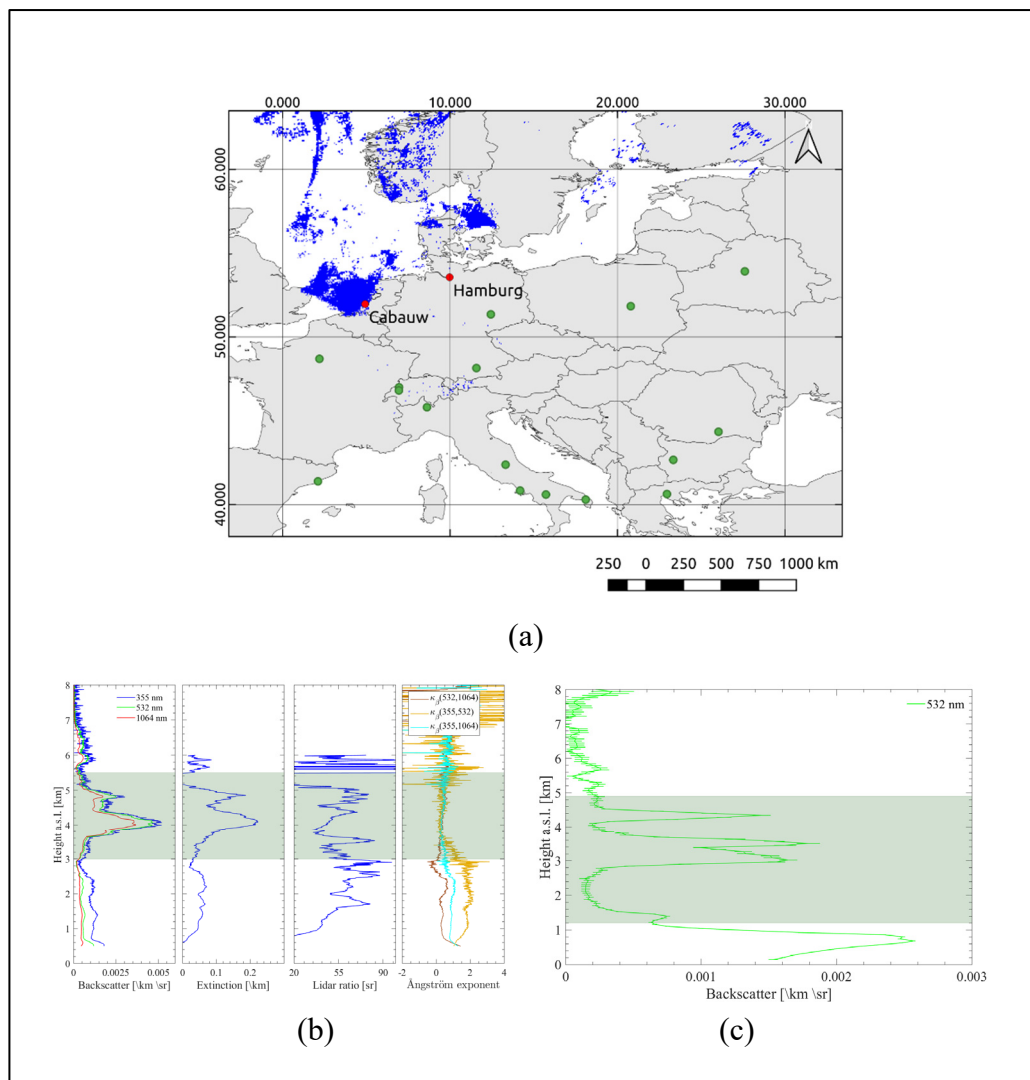
Figure 5. (**a**) Tailored RST$_{ASH}$ products of May 17 at 18:00 UTC and EARLINET measurement stations (in red) revealing the presence of ash, in green sites where no information was available. (**b**) Cabauw EARLINET aerosol backscatter coefficient, extinction coefficient, lidar ratio, and Ångström exponent profiles acquired the same day between 17:30–18:30 UTC. The green zone indicates the ash-affected portion of the profile. (**c**) Hamburg EARLINET aerosol backscatter coefficient acquired the same day between 17:30–18:30 UTC.

Figure 6a displays the tailored RST$_{ASH}$ product of May 18 at 12:00 UTC, showing the persistence of the ash phenomenon over Cabauw, in good agreement with information provided by EARLINET. The volcanic layer was observed in the 1.6–5.9 km a.s.l. range with a mean-layer backscatter coefficient at 532 nm of 0.25×10^{-6} m^{-1}sr^{-1} (Figure 6b) and a mean value of the Ångström exponent (532 nm/1064 nm) for the main aerosol layer between 3.6–4.4 km a.s.l. of 0.3 ± 0.2 (Figure 6c). Finally, Figure 6a shows that the RSTASH flagged a number of ash pixels even close to Ispra (Italy), where the ground-based lidar measurements, performed between 11:30–12:30 UTC, confirmed the presence of volcanic ash, with a mean-layer backscatter coefficient at 532 nm of 1.5×10^{-6} m^{-1}sr^{-1}, in the 2.2–8.6 km a.s.l. range (Figure 6d).

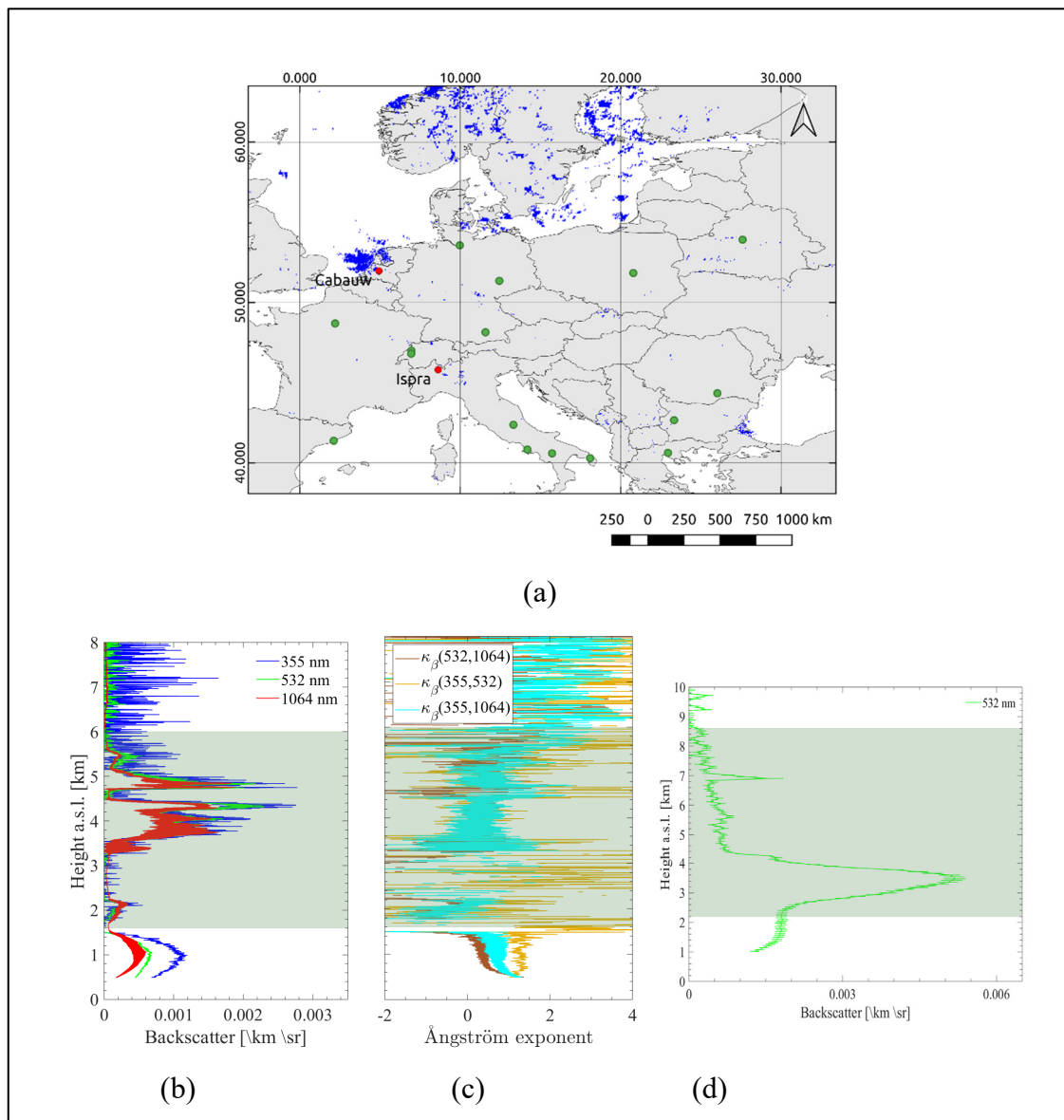**Figure 6.** (**a**) Tailored RST$_{ASH}$ products of May 18 at 12:00 UTC and EARLINET measurement stations (in red) generated using the same algorithm arrangement as Figure 5 and revealing the presence of ash in green sites where no information was available. (**b**) Cabauw EARLINET aerosol backscatter coefficient and (**c**) Ångström exponent profiles acquired the same day between 11:33–12:19 UTC. (**d**) Ispra EARLINET aerosol backscatter coefficient acquired the same day between 11:30–12:30 UTC. The green area indicates the dust-affected portion of the profile.

5. Discussion

In previous studies, we assessed the RST ash/dust products by means of comparison with independent, satellite-based products, namely the MODIS AOD at 550 nm products and CALIOP lidar profiles [25–27]. RST performance was then quantified in terms of false positive rate [35,38,39], demonstrating the important contribution offered by the used multi-temporal approach in detecting and tracking ash/dust plumes over wide areas, exploiting the large spatial coverage and high-temporal resolution of SEVIRI data.

In this work, we have carried out a first validation analysis of eRST$_{DUST}$ and RST$_{ASH}$ detections (including those from a recent tailored algorithm version) at local scale, using information provided by ground-based EARLINET quality assured lidar measurements. The latter corroborated RST ash/dust

detections at the investigated geographic locations, as summarized in Table 1, report the mean layer backscatter coefficient and the integrated backscatter at 532 nm, the aerosol type and the top/bottom altitude of the aerosol layer in reference to the analyzed SEVIRI data.

Table 1. eRST$_{DUST}$ and RST$_{ASH}$ detections corroborated by EARLINET lidar measurements. The mean-layer backscatter coefficient (β_{532}) at 532 nm along with the standard deviation, the layer integrated backscatter coefficient at 532 nm, the aerosol type, and the bottom-top layer height are provided by EARLINET. (*) The operating wavelength of the Sofia EARLINET station is 510 nm.

Satellite Data	Location	Algorithm	Mean Layer β_{532} (10^{-6} m^{-1} sr^{-1})	Layer Integrated β_{532} (sr^{-1})	Aerosol Type	Bottom-Top Height (km a.s.l.)
19/05/2008-21:00 UTC	Potenza	eRST$_{DUST}$	3.7 ± 0.9	0.0060	Mixed dust	1.4–3.3
20/05/2008-08:45 UTC	Thessaloniki	eRST$_{DUST}$	3.5 ± 0.1	0.0029	Mixed dust	1.4–3.3
20/05/2008-08:45 UTC	Sofia	eRST$_{DUST}$	1.2 ± 1.1*	0.0032	Mixed dust	1.6–4.3
16/04/2010-06:00 UTC	Hamburg	RST$_{ASH}$	6.0 ± 4.5	0.0258	Ash	0.7–5.2
17/05/2010-18:00 UTC	Cabauw	RST$_{ASH}$	1.9 ± 1.3	0.0030	Ash	3.0–5.5
18/05/2010-12:00 UTC	Cabauw	RST$_{ASH}$	0.2 ± 0.4	0.0014	Ash	1.6–5.9
18/05/2010-12:00 UTC	Ispra	RST$_{ASH}$	1.5 ± 1.5	0.0088	Ash	2.2–8.6

This study also shows that some ash/dust layers remained undetected because of overlying meteorological clouds, obscuring the ash/dust BTD signature. Regarding the cloud obstruction, clouds had a significant impact on the continuity of satellite observations. The intensity of the aerosol plume and the aerosol mixing also affected the identification of ash/dust clouds from space. In addition, Figure 4b shows that artefacts occurred even when the tailored RST$_{ASH}$ product was used, but to a lesser extent than the standard configuration.

Based on information from Tables 1 and 2 (where the characteristics of the ash/dust layers measured by EARLINET but undetected by satellite are reported), the mean-layer backscatter coefficient and layer integrated backscatter difference stand out. When not considering the cloud-affected cases, it seems the layer integrated backscatter coefficient threshold for a correct satellite identification is in the order of ~0.001 sr^{-1} m (except for the 18 May 2010 over Cabauw). All the considered cases had a layer integrated backscatter coefficient less than this threshold still remained undetected from space (Table 2). Similarly, the mean-layer backscatter coefficient around 10^{-6} m^{-1}sr^{-1} most likely acts as a threshold identification value. However, the number of study cases do not allow us to extract conclusive remarks and pinpoints the need to increase the examined cases. Furthermore, we think the aerosol mixing is an important factor in the aerosol satellite retrieval, although we cannot quantify this effect yet. We plan to extend our analysis with EARLINET, investigating the aerosol type mixing on satellite retrievals.

Additionally, the ash/dust aerosol backscatter coefficient is converted into the aerosol extinction coefficient with a constant lidar ratio of 50 sr. The constant value can be considered a good compromise for volcanic ash and Saharan dust [47,56]. The climate-relevant aerosol optical depth (AOD) is then estimated and given in Figure 7, with respect to successful/unsuccessful RST detections. Evidently and in agreement with Tables 1 and 2, our analysis highlights that the satellite detection is sensitive to the aerosol amount observed in the column. This analysis, providing quantitative information about detection limits of the RST-based algorithms, confirms the capacity of the used method in identifying ash/dust layers with a low AOD value. This potential was previously inferred by comparing RST results to independent satellite-based aerosol products [27,38].

Table 2. Ash/dust layers reported by EARLINET and undetected by RST ash/dust algorithms. The mean-layer backscatter coefficient (β532) at 532 nm along with the standard deviation, the layer integrated backscatter coefficient at 532 nm, the aerosol type and the bottom-top layer height are provided by EARLINET.

| Satellite Data	Location	Mean Layer β_{532} (10^{-6} m^{-1} sr^{-1})	Layer Integrated β_{532} (sr^{-1})	Aerosol Type	Bottom-Top Height (km a.s.l)	Issue
18/05/2008-10:00 UTC	Potenza	1.9 ± 1.0	0.0020	Mixed dust	1.8–2.8	Clouds
18/05/2008-21:00 UTC	Potenza	1.5 ± 0.7	0.0051	Mixed dust	1.4–4.8	Clouds
16/04/2010-06:00 UTC	Payerne	0.4 ± 0.1	0.0005	Ash	0.7–5.2	Plume features
17/05/2010-18:00 UTC	Hamburg	0.6 ± 0.5	0.0021	Ash	1.2–4.9	Plume features
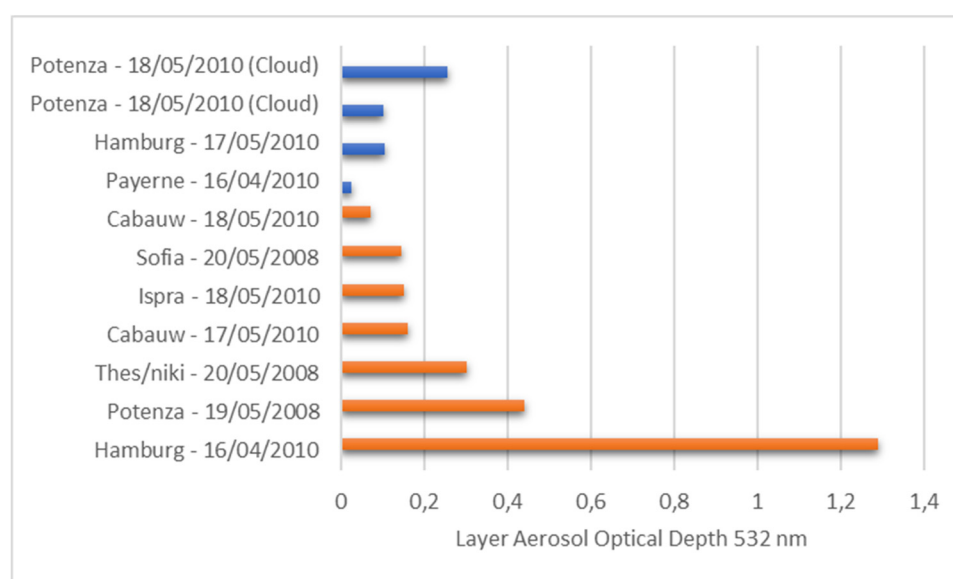
Figure 7. Ash/dust layer aerosol optical depth (AOD) at 532 nm as estimated by EARLINET aerosol backscatter measurements (cases reported in Tables 1 and 2). The backscatter coefficient to extinction coefficient conversion is made assuming a constant lidar ratio of 50 sr. The cases correctly detected by RST$_{ASH}$ and eRST$_{DUST}$ are reported in orange while the cases with no detection are reported in blue. A cloud label is reported for the cases in which ground-based stations identified clouds in the vertical column.

RST performance, coupled with the high temporal sampling of SEVIRI data (15 min), may be then exploited to provide timely and reliable information about ash/dust events. Therefore, the RST-based algorithms can promptly alert and initiate the non-automatic EARLINET stations. Figure 8 shows an example of this potential, displaying a time sequence (up to 15 min temporal sampling) of eRST$_{DUST}$ maps of May 20, 2008, generated between 07:15 UTC and 12:00 UTC, indicating that airborne dust affected, with a certain continuity, both Sofia and Thessaloniki sites. EARLINET measurements at Thessaloniki performed between 08:11–12:24 UTC confirmed information provided by eRST$_{DUST}$. EARLINET measurements started at Sofia 15 minutes later the Thessaloniki ones corroborated the presence of dust.

Thus, especially for Thessaloniki, the high frequency of SEVIRI observations would have enabled an efficient and prompt identification of airborne dust before the measurements were taken by the EARLINET station.
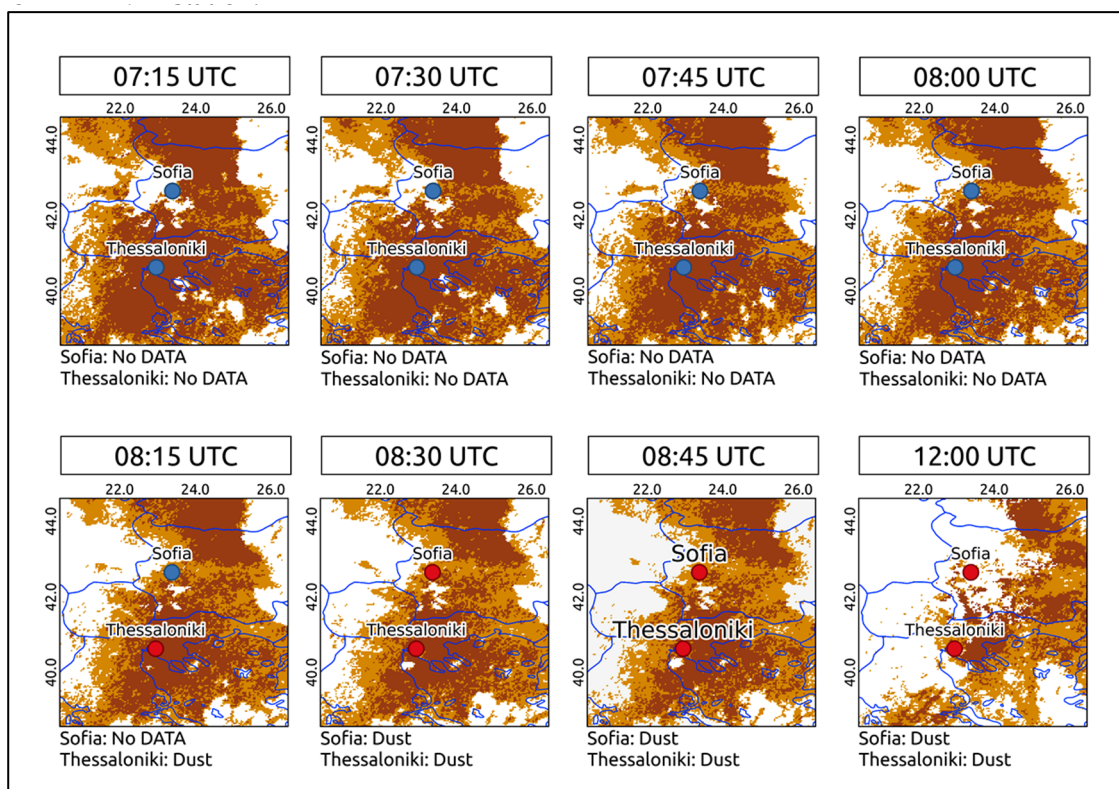
Figure 8. *e*RST$_{DUST}$ maps from SEVIRI data on May 20 between 07:15 UTC and 12:00 UTC. Red bullets indicate the time when lidar measurements were in progress at Thessaloniki and Sofia.

6. Conclusions

In the framework of the EUNADICS-AV project, we performed a first validation analysis of RST ash/dust detections at a local scale using ground-based EARLINET quality assured lidar measurements. Results achieved investigating two intense dust and ash events affecting the Mediterranean basin and continental Europe in May 2008 and April–May 2010, respectively, showed that the algorithms provided reliable information about the presence of ash/dust pixels on both daytime and nighttime satellite scenes. Moreover, the same analysis revealed some main limitations. First, there is a non-negligible impact of meteorological clouds, capable of obscuring the ash/dust BTD signature when the layers are below the cloud level. Second, there is sensitivity reduction which affects the algorithms in the presence of less intense aerosol layers. A preliminary detection limit has been found here in terms of integrated backscatter coefficient (aerosol backscatter coefficient), suggesting a threshold of ~0.001 sr^{-1} (~1 × 10^{-6} m^{-1}sr^{-1}), to allow successful ash/dust identification from space. Although further investigations are required to better understand and quantify the impact of these issues on the performance of the used RST-based algorithms, this paper confirms that SEVIRI data if properly analyzed may provide prompt and accurate information about the presence of ash/dust aerosols at specific sites of interest. A number of factors (e.g., changes in the SEVIRI pixel size, from 3 × 3 km at nadir up to about 10 × 10 km at the edges of the scan [56]) may affect performance of methods developed to detect ash/dust clouds from space. However, the RST-based algorithms comparing signals to those acquired under unperturbed conditions computed at pixel level, are capable of guaranteeing an increased sensitivity level towards ash/dust layers [25,37], which favors their usage at different spatial scales. Additionally, this work revealed the potential added value of using SEVIRI-based RST ash/dust maps as a "trigger" to switch on the EARLINET lidars in case of an impending airborne hazard. EARLINET, in fact, is primarily a research infrastructure and not an operational one, with station nodes that are not continuously in operation.

These results encourage the operational usage of the RST-based algorithms, including a tailored RST$_{ASH}$ version for the first time tested here, in supporting activities devoted to monitor and characterize ash/dust phenomena, complementing information from ground-based measurement systems. A synergistic use of both sources of information is very valuable, allowing for an integration of satellite-based, large scale, continuous and timely records with ground-based, accurate and quantitative measurements.

Author Contributions: A.F., F.M., L.M. and N.P. (Nikolaos Papagiannopoulos) wrote the manuscript. L.M. and F.M coordinated the work. A.F. and C.F. processed SEVIRI data. A.F. and N.P. (Nikolaos Papagiannopoulos) performed the validation analysis. S.T. contributed in editing the manuscript. N.P. (Nicola Pergola), G.P. and V.T. contributed resources and supervised the findings of this work. The interpretation of results was determined from discussions involving all authors. All authors have read and agreed to the published version of the manuscript.

Conflicts of Interest: The authors declare no conflict of interest.

References

1. Wen, S.; Rose, W.I. Retrieval of sizes and total masses of particles in volcanic clouds using AVHRR bands 4 and 5. *J. Geophys. Res. Atmos.* **1994**, *99*, 5421–5431. [CrossRef]
2. Herman, J.R.; Bhartia, P.K.; Torres, O.; Hsu, C.; Seftor, C.; Celarier, E. Global distribution of UV-absorbing aerosols from Nimbus 7/TOMS data. *J. Geophys. Res. Atmos.* **1997**, *102*, 16911–16922. [CrossRef]
3. Gangale, G.; Prata, A.J.; Clarisse, L. The infrared spectral signature of volcanic ash determined from high-spectral resolution satellite measurements. *Remote Sens. Environ.* **2010**, *114*, 414–425. [CrossRef]
4. Carlson, T.N.; Wendling, P. Reflected Radiance Measured by NOAA 3 VHRR as a Function of Optical Depth for Saharan Dust. *J. Appl. Meteorol.* **1977**, *16*, 1368–1371. [CrossRef]
5. Robock, A.; Matson, M. Circumglobal transport of the El Chichón volcanic dust cloud. *Science* **1983**, *221*, 195–197. [CrossRef]
6. Prata, A.J. Radiative transfer calculations for volcanic ash clouds. *Geophys. Res. Lett.* **1989**, *16*, 1293–1296. [CrossRef]
7. Prata, A.J. Observations of volcanic ash clouds in the 10–12 μm window using AVHRR/2 data. *Int. J. Remote Sens.* **1989**, *10*, 751–761. [CrossRef]
8. Zhang, P.; Lu, N.M.; Hu, X.Q.; Dong, C.H. Identification and physical retrieval of dust storm using three MODIS thermal IR channels. *Glob. Planet Chang.* **2006**, *52*, 197–206. [CrossRef]
9. Webley, P.W.; Dehn, J.; Lovick, J.; Dean, K.G.; Bailey, J.E.; Valcic, L. Near-real-time volcanic ash cloud detection: Experiences from the Alaska Volcano Observatory. *J. Volcanol. Geoth. Res.* **2009**, *186*, 79–90. [CrossRef]
10. Simpson, J.J.; Hufford, G.; Pieri, D.; Berg, J. Failures in detecting volcanic ash from a satellite-based technique. *Remote Sens. Environ.* **2000**, *72*, 191–217. [CrossRef]
11. Mosher, F.R. Four channel volcanic ash detection algorithm. In Proceedings of the 10th Conference on Satellite Meteorology and Oceanography, Long Beach, CA, USA, 9–14 January 2000; pp. 457–460.
12. Ellrod, G.P.; Connel, B.H.; Hillger, D.W. Improved detection of airborne volcanic ash using multi-spectral infrared satellite data. *J. Geophys. Res.* **2003**, *108*, 4356. [CrossRef]
13. Pergola, N.; Tramutoli, V.; Marchese, F.; Scaffidi, I.; Lacava, T. Improving volcanic ash cloud detection by a robust satellite technique. *Remote Sens. Environ.* **2004**, *90*, 1–22. [CrossRef]
14. Pavolonis, M.J.; Wayne, F.F.; Heidinger, A.K.; Gallina, G.M. A daytime complement to the reverse absorption technique for improved automated detection of volcanic ash. *J. Atmos. Ocean. Technol.* **2006**, *23*, 1422–1444. [CrossRef]

15. Ackerman, S.A. Using the radiative temperature difference at 3.7 and 11 μm to track dust outbreaks. *Remote Sens. Environ.* **1989**, *27*, 129–133. [CrossRef]

16. Wald, A.E.; Kaufman, Y.J.; Tanré, D.; Gao, B.C. Daytime and nighttime detection of mineral dust over desert using infrared spectral contrast. *J. Geophys. Res. Atmos.* **1998**, *103*, 32307–32313. [CrossRef]

17. Francis, P.N.; Cooke, M.C.; Saunders, R.W. Retrieval of physical properties of volcanic ash using Meteosat: A case study from the 2010 Eyjafjallajökull eruption. *J. Geophys. Res. Atmos.* **2012**, *117*, 1–14. [CrossRef]

18. Guéhenneux, Y.; Gouhier, M.; Labazuy, P. Improved space borne detection of volcanic ash for real-time monitoring using 3-Band method. *J. Volcanol. Geotherm. Res.* **2015**, *293*, 25–45. [CrossRef]

19. Naeger, A.R.; Christopher, S.A. The identification and tracking of volcanic ash using the Meteosat Second Generation (MSG) Spinning Enhanced Visible and Infrared Imager (SEVIRI). *Atmos. Meas. Tech.* **2014**, *7*, 581–597. [CrossRef]

20. Pavolonis, M.J.; Sieglaff, J.; Cintineo, J. Spectrally Enhanced Cloud Objects—A generalized framework for automated detection of volcanic ash and dust clouds using passive satellite measurements: 1. *Multispectr. Anal. J. Geophys. Res. Atmos.* **2015**, *120*, 7813–7841. [CrossRef]

21. She, L.; Xue, Y.; Yang, X.; Guang, J.; Li, Y.; Che, Y.; Fan, C.; Xie, Y. Dust Detection and Intensity Estimation Using Himawari-8/AHI Observation. *Remote Sens.* **2018**, *10*, 490. [CrossRef]

22. Albugami, S.; Palmer, S.; Meersmans, J.; Waine, T. Evaluating MODIS dust-detection indices over the Arabian Peninsula. *Remote Sens.* **2018**, *10*, 1993. [CrossRef]

23. Singh, J.; Noh, Y.J.; Agrawal, S.; Tyagi, B. Dust Detection and Aerosol Properties Over Arabian Sea Using MODIS Data. *Earth Syst. Environ.* **2019**, *3*, 139–152. [CrossRef]

24. Tramutoli, V. Robust satellite techniques (RST) for natural and environmental hazards monitoring and mitigation: Theory and applications. In Proceedings of the 2007 International Workshop on the Analysis of Multi-Temporal Remote Sensing Images, Leuven, Belgium, 18–20 July 2007. [CrossRef]

25. Sannazzaro, F.; Filizzola, C.; Marchese, F.; Corrado, R.; Paciello, R.; Mazzeo, G.; Pergola, N.; Tramutoli, V. Identification of dust outbreaks on infrared MSG-SEVIRI data by using a Robust Satellite Technique (RST). *Acta Astronaut.* **2014**, *93*, 64–70. [CrossRef]

26. Marchese, F.; Falconieri, A.; Pergola, N.; Tramutoli, V. A retrospective analysis of the Shinmoedake (Japan) eruption of 26–27 January 2011 by means of Japanese geostationary satellite data. *J. Volcanol. Geotherm. Res.* **2014**, *269*, 1–13. [CrossRef]

27. Marchese, F.; Sannazzaro, F.; Falconieri, A.; Filizzola, C.; Pergola, N.; Tramutoli, V. An Enhanced Satellite-Based Algorithm for Detecting and Tracking Dust Outbreaks by Means of SEVIRI Data. *Remote Sens.* **2017**, *9*, 537. [CrossRef]

28. Marchese, F.; Falconieri, A.; Pergola, N.; Tramutoli, V. Monitoring the Agung (Indonesia) Ash Plume of November 2017 by Means of Infrared Himawari 8 Data. *Remote Sens.* **2018**, *10*, 919. [CrossRef]

29. Marchese, F.; Falconieri, A.; Filizzola, C.; Pergola, N.; Tramutoli, V. Investigating Volcanic Plumes from Mt. Etna Eruptions of December 2015 by Means of AVHRR and SEVIRI Data. *Sensors* **2019**, *19*, 1174. [CrossRef]

30. Mona, L.; Pappalardo, G.; Amodeo, A.; D'Amico, G.; Madonna, F.; Boselli, A.; Giunta, A.; Russo, F.; Cuomo, V. One year of CNR-IMAA multi-wavelength Raman lidar measurements in coincidence with CALIPSO overpasses: Level 1 products comparison. *Atmos. Chem. Phys.* **2009**, *9*, 7213–7228. [CrossRef]

31. Pappalardo, G.; Mona, L.; D'Amico, G.; Wandinger, U.; Adam, M.; Amodeo, A.; Ansmann, A.; Apituley, A.; Alados Arboledas, L.; Balis, D.; et al. Four-dimensional distribution of the 2010 Eyjafjallajökull volcanic cloud over Europe observed by EARLINET. *Atmos. Chem. Phys.* **2013**, *13*, 4429–4450. [CrossRef]

32. Amiridis, V.; Kafatos, M.; Perez, C.; Kazadzis, S.; Gerasopoulos, E.; Mamouri, R.E.; Papayannis, A.; Kokkalis, P.; Giannakaki, E.; Basart, S.; et al. The Potential of the Synergistic Use of Passive and Active Remote Sensing Measurements for the Validation of a Regional Dust Model. *Ann. Geophys.* **2009**, *27*, 3155–3164. [CrossRef]

33. Gudmundsson, M.T.; Pedersen, R.; Vogfjörd, K.; Thorbjarnardóttir, B.; Jakobsdóttir, S.; Roberts, M.J. Eruptions of Eyjafjallajökull Volcano, Iceland. *Eos Trans. Am. Geophys. Union* **2010**, *91*, 190–191. [CrossRef]

34. Mona, L.; Amodeo, A.; D'Amico, G.; Giunta, A.; Madonna, F.; Pappalardo, G. Multi-wavelength Raman lidar observations of the Eyjafjallajökull volcanic cloud over Potenza, southern Italy. *Atmos. Chem. Phys.* **2012**, *12*, 2229–2244. [CrossRef]

35. Falconieri, A.; Cooke, M.C.; Filizzola, C.; Marchese, F.; Pergola, N.; Tramutoli, V. Comparing Two Independent Satellite-Based Algorithms for Detecting and Tracking Ash Clouds by Using SEVIRI Sensor. *Sensors* **2018**, *18*, 369. [CrossRef] [PubMed]

36. Cuomo, V.; Filizzola, C.; Pergola, N.; Pietrapertosa, C.; Tramutoli, V. A self-sufficient approach for Gerb cloudy radiance detection. *Atmos. Res.* **2004**, *72*, 39–56. [CrossRef]

37. Marchese, F.; Malvasi, G.; Ciampa, M.; Filizzola, C.; Pergola, N.; Tramutoli, V. A robust multitemporal satellite technique for volcanic activity monitoring: Possible impacts on volcanic hazard mitigation. In Proceedings of the 2007 International Workshop on the Analysis of Multi-temporal Remote Sensing Images, Leuven, Belgium, 18–20 July 2007; pp. 1–5. [CrossRef]

38. Piscini, A.; Corradini, S.; Marchese, F.; Merucci, L.; Pergola, N.; Tramutoli, V. Volcanic ash cloud detection from space: A comparison between the RSTASH technique and the water vapour corrected BTD procedure. *Geomat. Nat. Hazards Risk* **2011**, *2*, 263–277. [CrossRef]

39. Marchese, F.; Filizzola, C.; Mazzeo, G.; Pergola, N.; Sannazzaro, F.; Tramutoli, V. Assessment and validation in time domain of a Robust Satellite Technique (RSTASH) for ash cloud detection. *Geomat. Nat. Hazards Risk* **2011**, *2*, 247–262. [CrossRef]

40. A European Aerosol Research Lidar Network to Establish an Aerosol Climatology: EARLINET. Available online: https://www.earlinet.org/index.php?id=earlinet_homepage (accessed on 17 March 2020).

41. Aerosol, Clouds and Trace Gases (ACTRIS). Available online: https://www.actris.eu/default.aspx (accessed on 17 March 2020).

42. ACTRIS Data Center. Available online: https://actris.nilu.no/ (accessed on 17 March 2020).

43. *EARLINET Publishing Group 2000–2015: EARLINET VolcanicEruption 2000–2015*; 2018 World Data Center for Climate (WDCC)–DKRZ (Deutsches Klimarechenzentrum); World Data Center for Climate (WDCC): Hamburg, Germany, 2018. [CrossRef]

44. *EARLINET Publishing Group 2000–2015: EARLINET SaharanDust 2000–2015*; World Data Center for Climate (WDCC)–DKRZ (Deutsches Klimarechenzentrum); World Data Center for Climate (WDCC): Hamburg, Germany, 2018. [CrossRef]

45. Mona, L.; Liu, Z.; Müller, D.; Omar, A.; Papayannis, A.; Sugimoto, N.; Pappalardo, G.; Vaughan, M. Lidar Measurements for Desert Dust Characterization: An Overview. *Adv. Meteorol.* **2012**, *2012*, 1–36. [CrossRef]

46. Klein, H.; Nickovic, S.; Haunold, W.; Bundke, U.; Nillius, B.; Ebert, M.; Weinbruch, S.; Schuetz, L.; Levin, Z.; Barrie, L.A.; et al. Saharan dust and ice nuclei over Central Europe. *Atmos. Chem. Phys.* **2010**, *10*, 10211–10221. [CrossRef]

47. Wiegner, M.; Groß, S.; Freudenthaler, V.; Schnell, F.; Gasteiger, J. The May/June 2008 Saharan dust event over Munich: Intensive aerosol parameters from lidar measurements. *J. Geophys. Res. Atmos.* **2011**, *116*, 1–15. [CrossRef]

48. Tramutoli, V.; Marchese, F.; Falconieri, A.; Filizzola, C.; Genzano, N.; Hattori, K.; Lisi, M.; Liu, J.Y.; Ouzunov, D.; Parrot, M.; et al. Tropospheric and Ionospheric Anomalies Induced by Volcanic and Saharan Dust Events as Part of Geosphere Interaction Phenomena. *Geosciences* **2019**, *9*, 177. [CrossRef]

49. Winker, D.M.; Liu, Z.; Omar, A.; Tackett, J.; Fairlie, D. CALIOP observations of the transport of ash from the Eyjafjallajökull volcano in April 2010. *J. Geophys. Res. Atmos.* **2012**, *117*, 1–12.

50. Gudmundsson, M.T.; Thordarson, T.; Höskuldsson, Á.; Larsen, G.; Björnsson, H.; Prata, F.J.; Oddsson, B.; Magnússon, E.; Högnadóttir, T.; Petersen, G.N.; et al. Ash generation and distribution from the April-May 2010 eruption of Eyjafjallajökull, Iceland. *Sci. Rep.* **2012**, *2*, 572. [CrossRef]

51. Bolic, T.; Sivcev, Z. Eruption of Eyjafjallajökull in Iceland: Experience of European Air Traffic Management. *Transp. Res. Rec.* **2013**, *2214*, 136–143. [CrossRef]

52. Gislason, S.R.; Hassenkam, T.; Nedel, S.; Bovet, N.; Eiriksdottir, E.S.; Alfredsson, H.A.; Hem, C.P.; Balogh, Z.I.; Dideriksen, K.; Oskarsson, N.; et al. Characterization of Eyjafjallajökull volcanic ash particles and a protocol for rapid risk assessment. *Proc. Natl. Acad. Sci. USA* **2011**, *108*, 7307–7312. [CrossRef] [PubMed]

53. Langmann, B.; Folch, A.; Hensch, M.; Matthias, V. Volcanic ash over Europe during the eruption of Eyjafjallajökull on Iceland, April–May 2010. *Atmos. Environ.* **2012**, *48*, 1–8. [CrossRef]

54. Woodhouse, M.J.; Hogg, A.J.; Phillips, J.C.; Sparks, R.S.J. Interaction between volcanic plumes and wind during the 2010 Eyjafjallajökull eruption, Iceland. *J. Geophys. Res. Soild Earth* **2013**, *118*, 92–109. [CrossRef]

55. Stohl, A.; Prata, A.J.; Eckhardt, S.; Clarisse, L.; Durant, A.; Henne, S.; Kristiansen, N.I.; Minikin, A.; Schumann, U.; Seibert, P.; et al. Determination of time- and height-resolved volcanic ash emissions and their use for quantitative ash dispersion modeling: The 2010 Eyjafjallajökull eruption. *Atmos. Chem. Phys.* **2011**, *11*, 4333–4351. [CrossRef]

56. Mona, L.; Papagiannopoulos, N.; Basart, S.; Baldasano, J.; Binietoglou, I.; Cornacchia, C.; Pappalardo, G. EARLINET dust observations vs. BSC-DREAM8b modeled profiles: 12-year-long systematic comparison at Potenza, Italy. *Atmos. Chem. Phys.* **2014**, *14*, 8781–8793. [CrossRef]